Periodic mesoporous organosilica nanoparticles: Morphology control and sorption properties

Xavier Cattoën, Stéphanie Kodjikian, Philippe Trens

Periodic mesoporous organosilica nanoparticles: morphology control and sorption properties

Xavier Cattoën,[a,*] Stéphanie Kodjikian,[a] and Philippe Trens[b]

[a] Univ. Grenoble Alpes, CNRS, Grenoble INP, Institut Néel, 38000 Grenoble, France.
[b] ICGM, Univ Montpellier, CNRS, ENSCM, Montpellier, France
xavier.cattoen@neel.cnrs.fr

stephanie.kodjikian@neel.cnrs.fr

Philippe.Trens@enscm.fr

Abstract:

The synthesis of various periodic mesoporous organosilica nanoparticles (nanoPMOs) from the corresponding organo-bridged bis(triethoxy)silanes is described. A strong influence of the sodium hydroxide concentration is observed, leading to various sizes or morphologies depending on the precursor. In particular, in the case of the ethenylene linker, the morphology evolves from small flakes to elongated particles, while in the case of the phenylene precursor, small well-organized arms start to form at high base concentration. A mechanistic study shows that in all cases the nanoparticles nucleate before the condensation reaction commences and at very low conversions of the hydrolysis reaction of ethoxysilanes. The resulting hybrid nanoPMOs were compared for their adsorption properties towards rhodamine B (RB), which highlights large differences between the nanoPMOs with different linkers, and evidences a very strong affinity of the phenylene PMO with the poly-aromatic dye. Similarly, the sorption of cyclohexane and water revealed a much higher lipophilicity of the phenylene-bridged nanoPMO compared to the other studied linkers, despite a similar hydrophilicity. These results should help to better design nanoPMOs as nanovectors for drugs.

Keywords: Periodic mesoporous organosilica; Sol-Gel; Nanoparticle; gas sorption; adsorption.

Introduction:

Periodic mesoporous organosilicas (PMO) are mesoporous materials related to mesoporous silicas, but obtained from organo-bridged bis(trialkoxysilanes).[1,2] In their structure, of general formula RSi_2O_3, R being an organic bridging group, one fourth of the oxygen atoms of the silica structure is replaced by organic groups (Figure 1). Therefore, the variety of PMOs is virtually infinite as the organic bridging units may theoretically be varied at will. However, few structures have been described to date, since large or flexible organic linkers do usually not lead easily to mesoporous structures. The organic bridging group can either be seen as purely structural, or functional which enables application in optics,[3] catalysis, adsorption [4] or as drug carriers for nanomedicine.[5] For the latter application, it is often necessary to obtain the material as nanoparticles (NPs, < 150 nm), in particular for application in anti-tumor drug delivery. Therefore, the chemistry of PMO NPs, also called nanoPMOs, has to be developed.[6,7] Indeed, though much effort has been devoted over the past decade to the application of mesoporous silica nanoparticles (MSNs) as drug carriers, reports of nanoPMOs for drug delivery are much scarcer.[8] However, important advantages of nanoPMOs over silica have been reported, such as increased loading capacities for hydrophobic drugs,[9,10] lower hemolytic activity [11] or possible degradation of the NPs into small fragments when cleavable bridging organic units such as those containing disulfide or tetrasulfide functions are used.[8,10,12–14] Whereas numerous structures of MSNs have been reported to date, with variation in morphology, size or pore geometry,[15] the access to PMOs with sizes less than 150 nm is still difficult, and the structural variation is still at the early stage of research.[7,16–18] NanoPMOs with core-shell structures can be obtained by sol-gel hydrolysis-

condensation around pre-formed structures,[19,20] leading to hollow nanostructures after etching a silica core.[21] Similar structures were also obtained from emulsion droplets.[22] However, the direct sol-gel synthesis of nanoPMOs is still not well controlled to allow the formation of small size NPs,[23] or to tune the pore size and morphology. A single recent report has shown that catalyst concentration plays a role in the size control of nanoPMOs obtained from bis(triethoxysilyl)ethane and bis(triethoxysilyl)tetrasulfide to yield supermicroporous NPs.[13] Furthermore, despite the chemical diversity of the PMO nanostructures enabled by the variety of organic groups, no study has carefully compared the interfacial properties of different nanoPMOs with silica, and in particular their hydrophilic/hydrophobic balance. This is important to design nanostructures with optimized interfacial properties to encapsulate drugs or adsorb pollutants depending on their chemistry. In this study, we have explored the direct synthesis of various nanoPMOs with the aim of controlling their size and surface properties. In particular, a mechanistic study has been undertaken to understand the factors governing the formation of such nanoPMOs. Finally, the sorption of cyclohexane and water by various PMOs and MSN has been used to probe the hydrophilic/hydrophobic balance of such NPs, and to understand the increased interaction of the pore surface with rhodamine B (RB) in the case of the **Ph-PMO**.

Experimental Section:

Bis(triethoxysilyl)ethene (*E*/*Z* mixture, 4:1) was obtained by olefin metathesis from vinyltriethoxysilane, then distilled.[24] Bis(triethoxysilyl)benzene was prepared by a Barbier-Grignard reaction from TEOS and dibromobenzene, then distilled under reduced pressure.[25] Bis(triethoxysilyl)ethane was purchased from Acros, while CTAB, TEOS, and all other reagents were obtained from Sigma-Aldrich. Fresh sodium hydroxide solutions were prepared every day (2.0 M, NaOH). Gradient HPLC grade water (Fisher) was used in all syntheses. The reaction temperature was controlled within the reaction medium and was set to 80 °C ± 1 °C.

*Synthesis of **E-PMOs**:*

To a mixture of CTAB (250 mg, 0.69 mmol) and water (120 mL) placed in a 250 mL round bottom flask and stirred with a 20 mm × 40 mm olive stir bar was added sodium hydroxide (2.0 M in water, 600 µL, 1.2 mmol). The temperature was set to 80 ± 2 °C and the solution was stirred at 700 rpm. To this solution was added bis(triethoxysilyl)ethene (800 µL, 2.2 mmol). After 15 minutes, a condenser was adapted. 2 h after addition of the precursor, the obtained suspension was cooled, then centrifuged (41000 *g*, 20 min). The supernatant was discarded, the solid was dispersed in ethanol then the mixture was mildly sonicated to disperse the NPs. After centrifugation, the solid was placed in a round bottom flask with ethanol (30 mL) and aqueous hydrochloric acid (37%, 3 mL). The mixture was heated overnight at 75 °C, cooled to room temperature then centrifuged. The solid was washed twice with ethanol then dried in an oven at 60 °C.

*Synthesis of **Et-PMO**:* The same procedure was applied starting from bis(triehoxysilyl)ethane (800 µL, 2.2 mmol).

*Synthesis of **Ph-PMO**:* The same procedure was applied starting from bis(triehoxysilyl)benzene (862 µL, 2.2 mmol).

*Synthesis of **SiO_2**:* The same procedure was applied starting from TEOS (1.25 mL, 5.6 mmol).[26]

Adsorption of RB: To 0.500 mL of NP suspension (2.0 mg/mL) placed in a 1.5 mL plastic microtube were added an aqueous solution of RB hydrochloride (4.00 mg/mL or 0.200 mg/mL) and water, to reach a volume of 1.00 mL and a concentration of 2.00, 1.00, 0.30, 0.10, 0.040 or 0.020 mg/mL in RB and 1.0 mg in nanoparticles. For reference, the same experiments were repeated with pure water instead of NP suspension. The mixture was mixed with a vortex then left unstirred for at least 24 h at 20 °C. After centrifugation (5 min, 20 000 *g*) the supernatant concentration was analyzed by absorbance

spectroscopy. For these experiments, NPs with similar diameters of *ca* 90 nm were used, except for **E-PMO** where flakes obtained with [NaOH] = 6.7 mM were used.

Kinetics of RB adsorption: Similar experiments were performed after mixing a NP suspension (0.500 mL, 2.0 mg/mL), water (0.375 mL) and a RB solution (4.00 mg/mL, 0.125 mL) to reach a final concentration of 0.500 mg/mL in RB and 1.0 mg/mL in NPs. After a given time, the mixture was centrifuged (2 min, 20 000 *g*) and the supernatant concentration was determined by absorbance spectroscopy.

Characterization: For field effect scanning electron microscopy (FE-SEM) imaging, a Zeiss Ultra+ scanning electron microscope was used with a voltage of 3 kV at a working distance of 3 mm. The samples were prepared by drying droplets (3 µL) of a dilute NP suspension on a doped silicon wafer. Transmission electron microscopy (TEM) was performed on a Philips CM300 microscope working at 300 kV. The images were obtained thanks to a TemCam F416 TVIPS camera (4k × 4k, 16 bits). Other images were obtained using a JEOL NEOARM (200 kV) microscope equipped with a GATAN Oneview Camera (4k × 4k, 16 bits). For sample preparation, a dilute drop of NP suspension in ethanol was deposited on a carbon-coated copper grid. Nitrogen sorption experiments were conducted at a temperature of 77 K using a Micromeritics Tristar 3000 apparatus. Prior to the experiments, the samples were activated for 12 hours at 80 °C under a secondary vacuum pressure of 10^{-3} Pa. The specific surface areas were determined by applying the BET model within the range of $0.05 < p/p° < 0.15$, with a cross-sectional area of 0.162 nm^2 considered for the adsorbed nitrogen molecules. Due to the significant uptake of nitrogen observed at low relative pressures in the sorption isotherms, the pore size distributions were further analyzed using a DFT derivation on the adsorption branches of the isotherms. It should be noted that the more traditional BJH model cannot be accurately applied for quantifying small mesopores diameters. [27] In the DFT derivation, we chose to model the pores as cylinders. The total pore volumes were estimated at $p/p° = 0.6$ and hydraulic volumes were calculated taking 647 as ratio between perfect gas and liquid nitrogen molar volumes at 77 K. To monitor the pH, a SevenEasy pHmeter from Mettler Toledo was used, with a pH inlab expert electrode working from 0 to 95 °C. The time resolution was 1 s. Thermogravimetric analyses (TGA) were carried out on a SETARAM TAG 16 instrument. 7-10 mg samples were placed in alumina crucibles, and the experiments were conducted under an oxygen atmosphere with a heating rate of 10 °C min^{-1}. Zeta potentials (ζ) were determined in 1 mM acetate or phosphate buffers using a Wallis analyzer (Cordouan, France), after checking that the size determined by dynamic light scattering using the cumulant fit was lower than 200 nm (DLS, fit in intensity measured on a Cordouan Nanokin apparatus). Absorbance spectra were registered using a SAFAS Xenius XC cuvette spectrofluorometer. FTIR spectra were measured in transmission on a Thermo Fisher Nicolet™ iN™10 spectrometer on KBr pellets. Water and cyclohexane isothermal sorption analyses were conducted using a DVS Resolution apparatus manufactured by Surface Measurements Systems in London, UK. This instrument enables precise measurement of sorption isotherms at various temperatures and within a predetermined range of partial pressures. This microbalance can detect changes in sample mass as low as 0.1 µg. The measurement pans are connected to the microbalance through hanging wires, situated in a double chamber, which is housed in a temperature-controlled cabinet. To maintain a constant partial pressure of vapor, a continuous stream of dry nitrogen gas (100 mL/min) mixed with another nitrogen stream containing the vapor is passed through the chambers. A typical experimental run begins under isothermal conditions, starting from 0% partial pressure and incrementally increasing to 95% in successive steps of 5%. The process is then reversed, decreasing back to 0% in the same stepwise manner. These incremental steps of partial pressures in the nitrogen vapor mixture are employed to determine the complete sorption isotherm. Each adsorption-desorption cycle lasts approximately 6 days. The equilibrium criterion is determined based on the slope of the mass versus time curve. Specifically, the parameter dm/dt is set to 0.008%, resulting in an approximate time requirement of 8 hours for each partial pressure step. All the experiments were conducted at 25 °C. Cyclohexane (99.9%) was purchased from Sigma-Aldrich. Deionized water was used. Both sorbates were degassed under nitrogen flow before use.

Results and discussion:

Et-PMO NPs were prepared using a sol-gel procedure promoted by NaOH at 80 °C using CTAB as structure-directing agent and were obtained as nearly spherical objects (Figure 2). Though the size of the obtained NPs was almost independent of the stirring speed and reaction temperature,[28] the effect of starting pH was very strong. Starting from an initial concentration of 14.6 mM of NaOH,[29] the concentration of sodium hydroxide was decreased incrementally to 7 mM. A clear trend shows that by decreasing the catalyst concentration, the size decreased accordingly, enabling to tune the NPs diameter from 345 nm to 85 nm. Such a trend is surprising at first glance, as the increase of the catalyst concentration should result in an increase of nucleation rate, thus in smaller NPs. However, this effect has already been observed for the preparation of MCM-41-type MSNs,[30,31] and recently explained by an effect of ionic strength rather than nucleation speed.[32] Indeed, by adding increasing amounts of sodium chloride at the same initial pH, the authors reported an increase of the MSNs size. A similar experiment was performed here, with the addition of various amounts of sodium chloride to reach ionic strength of 14, 18 and 22 mM leading to final NPs diameters of 90, 135 and 160 nm, respectively (Figure 2). Additionally, the NPs size could be decreased by decreasing the initial concentration of **Et** precursor. The pore structure in these NPs could be attributed to the *Pm*3*n* space group, for the largest NPs with a unit cell parameter $a_0 \simeq 10.9\ nm$. For smaller sizes, the diffraction peaks broaden as a result of a weakening of the structural organization (Figures 3 and S1). Transmission electron microscopy (TEM, Figure 2) on **Et-PMOs** obtained from [Et]=18 mM and [NaOH]= 8.3 mM clearly reveals the presence of a porous structure but without a noticeable organization as already deduced by PXRD for these small NPs.

Interestingly, the evolution of the size and morphology for the **E-PMOs** is rather different than for the **Et-PMOs** (Figure 4). Although at high sodium hydroxide concentration the reported bean-like morphology with longitudinal porosity was confirmed,[10] upon decreasing the sodium hydroxide concentration the aspect ratio of the NPs drastically decreased with the formation of spherical objects at intermediate concentrations and of unprecedented PMO flakes at low concentration (8.3 mM). Meanwhile, the diameter of the NPs remains in the 120-180 nm range, thus much less affected than in the case of the **Et-PMOs**. The PRXD diffractograms for all samples (Figures 3 and S2) exhibit at least three different peaks at q_0, $\sqrt{3}\ q_0$ and $2\ q_0$, with $q_0 \simeq 1.5\ nm^{-1}$, which agrees with a 2D hexagonal (*P*6*mm*) arrangement of pores [33] with a pore-to-pore distance a_0 of *ca* $4.8\ nm$. This is slightly larger than for the corresponding mesoporous silica nanoparticles of similar 2D hexagonal symmetry and obtained with the same surfactant (where $a_0 \simeq 4.6\ nm$).[34] For the **E-PMO** flakes, TEM micrographs show the presence of pores with a regular organization, as evidenced by the Fast Fourier Transform of the image which shows a hexagonal pattern (Figure 4).

Starting from a phenylene linker, a trend similar to that of **Et-PMO** NPs was observed (Figure 5). At low hydroxide concentration, small NPs with a rough surface were obtained, with increasing size until 16 mM. Surprisingly, for larger hydroxide concentrations, small arms start to form. This type of morphology was already observed for NPs grown on silica or polystyrene and modified with amino groups,[21,35] but also for **Ph-PMO** based NPs, with arms formed from another precursor (**Et** or **E**).[36,37] Though under the conditions used in the latter studies no arms were observed for the **Ph-PMO** core alone,[36] this result indicates that the **Ph-PMO** itself is prone to grow with a multipodal architecture. For this composition, the increase of the ionic strength of the medium obtained by addition of sodium chloride led to a slight decrease of the average diameter, but much less than that observed for silica or **Et-PMO**. Small angle XRD led in all cases to broad patterns, reminiscent of the wormlike morphology observed for the reported **Ph-PMO** NPs (Figures 3 and S3). Interestingly, the TEM micrographs obtained for nanospheres revealed a local organization of the pores, with parallel channels. Similarly, for multipodal nanoparticles the arms also feature parallel channels (Figure S4), though no such organization can be detected by PXRD, where only a broad signal is observed as a result of a major disordered structure.

The FTIR spectra of the materials (Figure S5) agree with the expected structure. The large band between 1000 and 1200 cm^{-1} evidences the formation of an extended siloxane network after the sol-gel hydrolysis and condensation of the organo(triethoxy)silane precursors. The sharp bands at *ca* 1160 cm^{-1} indicate the presence of Si-C linkages, while the organic functions are characterized by C-H stretching bands at 2980 (**E-PMO**), 2870-2940 (**Et-PMO**) and 3060 cm^{-1} (**Ph-PMO**). The FTIR spectra of nanoPMOs also show the absence of sharp CH_2 stretching peaks at 2848 and 2915 cm^{-1}, which are the signature of the CTAB surfactant, thereby indicating the success of its removal from the pores by the acidic extraction procedure. Moreover, the thermogravimetric analyses (TGA) also agree with the $O_{1.5}Si\text{-}R\text{-}O_{1.5}$ formulae for these NPs, with weight losses corresponding well to the calculated ones (Figure S6). It is noteworthy that **Ph-PMO** possesses an extraordinarily high thermal stability, as already described for similar materials.[37,38]

The nitrogen sorption isotherms obtained with the PMOs are of the type IV, according to the IUPAC classification (Figure 6). They all share the same features relevant to mesoporous materials. Indeed, they exhibit a clear uptake at intermediate relative pressure, followed by a rather flat saturation plateau. They also show differences, in terms of adsorbed amounts, but also in terms of location of the capillary condensation process. After DFT analysis of the adsorption branches of the three sorption isotherms, different pore size distributions have been obtained ranging from 2.9 nm up to 3.8 nm for **Ph-PMO** and **E-PMO** respectively, whereas **Et -PMO** has an intermediate pore size of 3.4 nm. These pore diameters are consistent with the location of the nitrogen uptake, the lowest relative pressure corresponding to the material with the smallest pore diameter. At very high relative pressures, slight hysteresis loops can be seen on **E-PMO**, **Et-PMO** and **SiO_2**. This feature can be attributed to some interparticular porosity. The textural properties of the different materials have been gathered in Table 1. The silica material **SiO_2** has a nitrogen sorption isotherm reminiscent of the type IV. However, the pores filling occurs at very low relative pressure, which corresponds to very small mesopores. According to the DFT derivation, the pore size distribution is centered around a pore diameter of 2.3 nm. Our approach thus leads to the preparation of PMOs characterized by their populations of small mesopores. In the literature, few studies have shown the preparation of similar materials, with the porosities being usually in the micropores range which is less appropriate for encapsulating systems. For instance, Guan *et al* could produce materials characterized by a wide range of supermicropores as the curvature of the nitrogen sorption isotherms clearly changed at p/p° located between 0.2 and 0.3.[7] The average pore diameters of the materials obtained in this reference [7] ranged between 1.1 nm and 1.5 nm for the largest. In fact, these sorption isotherms belonged to the type I more than the type VI which was quite surprisingly suggested by the authors. Type I is typical for microporous materials and all the materials produced in that paper were therefore supermicroporous with rather wide pore size distributions. The difference between these materials and the present PMOs must be stressed as it is a key point in terms of applications.[10,29]

The large variety of morphologies and pore structures observed depending on the nanoPMO precursor may arise from different mechanisms of formation. To this aim, the initial stages of the formation of PMO NPs were followed *in situ* by monitoring the pH of the solution in the reaction vessel itself, in order not to disturb the physico-chemical processes, according to a protocol recently developed by our research group.[26] Indeed, the pH evolution under basic activation is related to the amount of hydroxide (OH^-) anions consumed or formed during hydrolysis and condensation reactions, respectively, as shown by equations (1-3).

Hydrolysis: $\equiv Si\text{—}OEt + OH^- \rightarrow \equiv Si\text{—}OH + EtO^- \rightarrow \equiv Si\text{—}O^- + EtOH$ (1)

Condensation: $\equiv Si\text{—}O^- + \equiv Si\text{—}OEt + H_2O \rightarrow \equiv Si\text{—}O\text{—}Si\equiv + EtOH + HO^-$ (2)

$\equiv Si\text{—}O^- + \equiv Si\text{—}OH \rightarrow \equiv Si\text{—}O\text{—}Si\equiv + HO^-$ (3)

In all cases, and similarly to what was found for silica, a linear decrease of the pH is first observed, before abruptly reaching a plateau (Figure 7).[26] Experimentally, the end of the linear decrease corresponds to the cloud point when the mixture becomes turbid. Then the pH starts again to decrease with a lower slope, before gradually increasing again. The slope of the initial pH decrease, related to the kinetics of the first hydrolysis of the alkoxysilane is much lower for the PMO precursors than for TEOS (Table 2). This trend may be related to the electron density at silicon, as the alkyl groups in organosilanes are more electron-donating than the ethoxide substituent, thereby destabilizing the negatively charged silicon atom in the pentacoordinated reaction intermediate of the S_N@Si reaction.[39,40] Similarly, the sp^2 carbon atoms of the phenylene and ethenylene substituents of the **Ph** and **E** precursors enable a better stabilization of the pentacoordinated intermediates than the sp^3 carbon of **Et** because of their higher electronegativity, thereby increasing the reaction rate. Another striking difference between silica and PMOs is the pH at which the nucleation of the micelles-silane nanoparticles occurs. From the determined pH difference, the hydroxide consumption thus the amount of singly hydrolyzed silicon atoms at the cloud point can be determined (Table 2). All these observations highlight that the PMO NPs are formed during the early stages of the synthesis, with a nucleation event at *ca* 30 s in all cases. At this stage, nanospheres or nanorods of inflated CTA^+ micelles and silanolates would be formed and self-assemble into larger nanostructures. As the silanolates and ethoxysilanes molecules come closer, the rate of condensation would dramatically increase, as noted by the flattening of the pH curve. The lower pH difference at the nucleation point is an indication that the nucleation takes place at a lower conversion for the PMOs with respect to silica, as only 8-10% of the silicon atoms feature a hydrolyzed ethoxy group. This effect may be related to the higher hydrophobicity of the organosilyl groups compared to the ethoxysilyl leading to an easier precipitation of the micelle-silanolate assemblies. However, whereas the electronic effects of the substituents at silicon enable a good understanding of the kinetics of formation, the impact of the precursor on the morphology and on the pore arrangement cannot be fully understood at this point.

The impact of the electronic and structural differences of the PMO NPs was probed by the encapsulation of rhodamine B (RB), a cationic polycyclic aromatic dye.[28,37] Incubation of well-dispersed NPs in an aqueous RB solution at 0.5 mg/mL in dye and 1.0 mg/mL for NPs led to encapsulation efficiencies varying from 17% for **Et-PMO** to 25 for **SiO_2**, 34 and 65% for the **E-** and **Ph-PMOs**, respectively after 24 h. These values point out to a much higher affinity of the organic cationic dye with the organosilica walls with respect to pure silica. For this study, kinetic effects due to diffusion limitations can be ruled out as the equilibrium is reached within 10 minutes (Fig S7). To better understand the differences between sorbents, we performed RB adsorption isotherms at 293 K by varying the dye concentration. Several models can be used to interpret adsorption equilibrium data, which compare how adsorbate molecules are distributed between the adsorbent and the liquid phase and describe the equilibrium adsorption capacity of adsorbents. When designing an optimized adsorption system for dye removal, it is crucial to fit adsorption data to the most appropriate sorption isotherm model. In this study, we analyzed the experimental equilibrium data of RB adsorption onto NPs using three sorption models: Langmuir, Freundlich and Temkin. These expressions establish the relationship between the equilibrium concentration of adsorbate in the bulk liquid phase (C_e) and the dye uptake per unit mass of adsorbent (q_e) at a constant temperature.

The Langmuir isotherm model is suitable for describing the adsorption of a fully covered monolayer of adsorbate species on a uniform surface of adsorbent, assuming constant energy and no interaction among adsorbed species. The Langmuir isotherm can be expressed linearly as:

$$\frac{C_e}{q_e} = \frac{1}{q_{max} K_L} + \frac{C_e}{q_{max}} \quad (4)$$

where the constants q_{max} and K_L represent the maximum adsorption capacity of the adsorbent for the monolayer and the energy or heat of adsorption, respectively. The Langmuir adsorption equilibrium

constant (K_L) is indicative of the binding site affinity, with higher values indicating stronger adsorption bonds. [27,41] By plotting C_e/q_e against Ce and analyzing the intercept and slope, the values of K_L and q_{max} for different materials were determined (Equation 4 and Figure S8). From the Langmuir isotherm, an additional useful parameter called the separation factor (R_L) can be obtained. R_L is a dimensionless constant given by $R_L = 1/(1 + K_L C_o)$, where C_o represents the initial dye concentration. The R_L value allows prediction of the adsorption isotherm type, such as irreversible ($R_L = 0$), unfavorable ($R_L > 1$), linear ($R_L = 1$), or favorable ($0 < R_L < 1$). [42] In all systems studied, R_L values ranged from 0 to 1 as the initial concentration of RB dye varied from 0.2 to 2.0 mg/mL at the specified temperature, indicating a favorable adsorption process between RB and NPs (Table 3). The lowest R_L values were observed at higher initial concentrations, approaching saturation. This observation is consistent with the expectation that sorbate/sorbent interactions would be weaker near saturation compared to the initial stages of the sorption process.

The Freundlich isotherm model postulates that the adsorbate can undergo adsorption in multiple layers on a heterogeneous surface of the adsorbent, characterized by varying energy sites and affinities. This model considers the mutual interaction among the adsorbed molecules. [43,44] The linear Freundlich isotherm can be written according to the following expression:

$$\log[q_e] = \log[K_F] + \frac{1}{n}\log[C_e] \quad (5)$$

Plotting $\log[q_e]$ versus $\log[C_e]$ (Equation 5) provides the Freundlich constant (K_F) and heterogeneity factor (n). The constants n and K_F are the measures of the adsorption strength and adsorption capacity, respectively. A value of n between 2-10, around 1, or lower than 1 indicates a favorable adsorption, moderately difficult adsorption, or poor adsorption, respectively. The values of n and K_F calculated from the Freundlich isotherms are reported in Table 3. These results from the Freundlich isotherm analysis support favorable adsorption and effective interaction between RB and NPs, regardless of the nature of the spacer. The corresponding regression coefficient values located between 0.9074 and 0.9834 indicate a good fit of experimental equilibrium data with the Freundlich isotherm model, but a poorer fit than when using the Langmuir model. Indeed, in the case of the Langmuir model, the correlation coefficients were located between 0.9311 and 0.9958. However, in the case of **Et-PMO**, the Freundlich model gives a better correlation coefficient. It can be supposed that for this particular material, lateral interactions and surface heterogeneities cannot be neglected. Finally, the Temkin model was tested on these materials, but gave inconsistent results (Table S1)

It can be concluded that among the models considered, the Langmuir isotherm leads to the best representation of the sorption process. For confirming the appropriateness of the Langmuir model, it can be noted that the calculated q_{max} closely match the actual experimental values for all the materials. In all cases, the interaction between **Ph-PMO** and RB appears much higher than with the other materials. The affinity constants are in the order **Ph**>>**E**>**SiO$_2$**>**Et**, and should be related to strong interactions between the hosts and the polycyclic aromatic cationic dye (Table 3). The affinity constant of RB with **Ph-PMO** is indeed in the order of magnitude of fully hydrophobized silica aerogels,[45] but with a loading at saturation, q_m three times higher (see Table S2). It is interesting to note that their surface chemistry is similar while their sorption capacity favor **Ph-PMO**. To better understand the interaction between the cationic dye and the nanomaterials, we determined the Zeta potential of the NPs depending on the pH (Figure S9). The points of zero charge could be determined, with values of *ca* 4.0, 3.0, 5.5 and 3.0, for **E**, **Et**, **Ph** and **SiO$_2$**, respectively. Some of these results agree with a recent report highlighting a large shift of the isoelectric point from 2.5 to 6.5 when coating MSNs with a layer of **Ph-PMO**.[20] It is noteworthy that the materials with higher affinity for the cationic dye are those with the highest points of zero charge, thus the least negative Zeta potential at neutral pH, which indicates that electrostatic

forces are not the dominant interaction favoring the adsorption of the dye. Therefore, we believe that van der Waals forces and π-stacking interactions between the double bonds in **E**- and **Ph-PMO** and the polycyclic aromatic compound are determining factors that govern the affinity between adsorbent and adsorbate.

Adsorption studies in the gas phase using cyclohexane and water as adsorbate were further used to reveal the lipophilic or hydrophilic character of these materials.[46] Water is an ideal probe for detecting polar surface sites with which hydrogen bonding can form. Because of its small weight, this interaction is the most intense, provided that the surface has polar sites. On the other hand, cyclohexane only generates dispersive interaction whose intensity is correlated to its molar mass. In this sense, the combination of these two probes provides us with a rather precise picture of the surface chemistry of the different materials. The sorption isotherms of cyclohexane and water at 25 °C by the different materials can be found in Figure 8 (left) and in Figure 8 (right), respectively. Looking at Figure 8 (left), the cyclohexane sorption isotherms appear quite close to the nitrogen sorption isotherms in terms of general shape. Obviously, these materials are mesoporous, with pores ranging between 2 and 3.5 nm, and cyclohexane adsorption does not change these textural parameters. In the case of cyclohexane, capillary condensation can be seen at relative pressures located between 0 and p/p° = 0.3. These are therefore downshifted compared to the capillary condensation obtained with nitrogen, which is consistent with former studies that showed that the nature of the sorbate, through its surface tension, strongly influences its condensation.[47–49] Additionally, the mesopores filling processes occur as observed for nitrogen. Indeed, capillary condensation first occurs in **SiO_2** small mesopores, followed by **Ph-PMO**, **Et-PMO** and finally, **E-PMO**. The sorption capacities at saturation are also in the same order as found for nitrogen. **E-PMO** exhibits a distinct hysteresis loop which can be explained by cavitation effects as usually described for nitrogen. If the hysteresis loops are almost absent in the case of **Ph-PMO**, **Et-PMO** and **SiO_2**, it is due to the very small size of the mesopores in these materials.[50] The slope at very low relative pressure is high which suggests a high affinity of the PMOs for cyclohexane. As the ligands are organic, it is quite understandable that cyclohexane is able to interact with the ligands in a favorable fashion. From these slopes, Henry's constants can be calculated, which are gathered in Table 1. **E-PMO** and **Et-PMO** have very similar Henry's constants which is consistent with the surface chemistry of these two materials. Indeed, the two ligands likely induce comparable interaction with cyclohexane. In the case of **Ph-PMO**, the Henry's constant is higher which can be interpreted by the strong interaction between the aromatic ligand and cyclohexane. Furthermore, its mesopores are smaller in size, which induces stronger confinement effects. In the case of **SiO_2**, despite an even higher confinement effect due to the presence of very small mesopores, the Henry's constant is lower as cyclohexane only interacts with pure silica. In the case of Aerosil 200, which is a non-porous silica, a Henry's constant of 41 $mg.g^{-1}$ was obtained using *n*-hexane, thus showing the influence of confinement effects.[51]

The sorption isotherms obtained with water are represented in Figure 8 (right). At first glance, the shape of the curves is different to those observed in the case of cyclohexane. Large hysteresis loops are present for all materials, even for **SiO_2**. However, the desorption branches reach the adsorption branches at very low relative pressure. In this region, the slopes of the sorption isotherms are moderate. As mentioned above, the PMOs are mesoporous and water adsorption should proceed according to the same sorption processes as for cyclohexane. The capillary condensation can be estimated using the Kelvin equation which can be written as follows:

$$\ln\left(\frac{p}{p^o}\right) = -\frac{2\gamma V_m}{r_k \mathrm{RT}} \quad (6)$$

The surface tension of water is 72 $mJ.m^2$ for water against 24.4 $mJ.m^2$ for cyclohexane at 25 °C.[52] At the same temperature, the molar volumes are 0.018 $L.mol^{-1}$ and 0.108 $L.mol^{-1}$ respectively. In mesopores of 2.5 nm Kelvin diameter, capillary condensation should occur in the region of $p/p° = 0.18$ in the case of cyclohexane whereas it should occur close to $p/p° = 0.95$ in the case of water. This calculation is consistent with the results obtained, thus confirming that the large water uptakes at higher relative pressures correspond to water condensation in the mesopores of the PMOs. Regarding the slopes at low relative pressures, the Henry's constants obtained after water adsorption are also reported in Table 1. They are much lower than in the case of cyclohexane, which suggests a rather poor hydrophilicity of the three PMOs. We already noticed that the branches of the sorption isotherms are superimposed at very low relative pressure. It can be deduced that water can be completely removed from these materials, which can be understood as we pointed out their rather poor hydrophilicity. Performing cyclohexane sorption after water sorption on the very same samples after a short degassing stage led to very similar sorption isotherms. As emphasized above, the organic linkers play a central role in sorbate/PMO affinity. The lipophilic linkers thus reduce the hydrophilic character of the PMOs, though this character can only be annihilated by silylation of the remaining silanol functions.[53] In the case of **SiO_2**, the presence of a higher density of surface silanols leads to an increase of the correspondent Henry's constant. This value remains lower than that obtained in the case of cyclohexane sorption by **SiO_2**. This can be understood by considering that **SiO_2** has been activated at high temperature, leading to a dihydroxylation of the **SiO_2** surface. This material therefore has an equilibrated hydrophilic/hydrophobic balance. Additionally, it is of interest to compare water and cyclohexane amounts at saturation. As the PMOs are lipophilic and poorly hydrophilic, one could think that the PMOs adsorb more cyclohexane than water molecules. For a clearer discussion, the sorption isotherms can be shown as $mmol.g^{-1}$ instead of $mg.g^{-1}$. As an example, we can focus on **Ph-PMO** which has clear saturation plateaus for water and cyclohexane. They are located at 33 $mmol.g^{-1}$ and 6.1 $mmol.g^{-1}$ respectively. It is therefore possible to adsorb 5.5 times more of water molecules compared to cyclohexane. Considering the molecular volume of these two probes at 25°C, values of 30 A^3 and 180 A^3 can be obtained for water and cyclohexane respectively, leading to a ratio of 6. This ratio is very close to the ratio obtained considering the saturation plateaus which confirms that the materials can be completely filled by water or cyclohexane, regardless of the hydrophilic/hydrophobic balance of the materials.

Conclusion:

NanoPMOs featuring ethylene, ethenylene or phenylene linkers can thus be obtained under various morphologies depending on the precursor used, and on the amount of sodium hydroxide. This control of the size and morphology is fundamental for application in nanomedicine. While spherical NPs of controllable size with a *Pm*3*n* cubic pore arrangement were obtained for the ethylene-linked PMOs, thin to elongated NPs can be made from the ethenylene-bridged precursor, with a *P*6*mm* pore arrangement. Interestingly, the phenylene-bridged precursor led to spherical NPs but also to multipodal structures upon variation of the sodium hydroxide concentration. Interestingly, the mechanism of formation of these NPs follows the same path as for MSNs, but with slower hydrolysis kinetics while the nucleation of NPs occurs earlier in the reaction process. Accordingly, kinetic factors such as the shape of the surfactant-silicates micelles at the moment of nucleation may thus direct the geometry of the pore assemblies, so that the final texture of the NPs depends more on this parameter rather than on the preferred arrangement of the surfactant itself in free solution. Further investigations using additives are needed to fully clarify this point.[54] In all cases, we were able to obtain NPs with a mesoporous texture and DFT pore sizes between 2.9 and 3.8 nm, by contrast to already published synthetic protocols[7] where the pore size ranged between 1.1 and 1.5 nm in the micropores range. These larger pore sizes should lead to improved loadings of large molecular compounds. We thus tested the encapsulation of RB on the PMOs, with **Ph-PMO** giving the largest affinity constant compared to the other structures.

This evidences that among the advantages of nanoPMOs over MSNs for nanomedicine, the introduction of organic groups within the structure can lead to strong improvement for the encapsulation of hydrophobic molecules. To clarify this point, the interfacial properties of the different PMOs were probed by cyclohexane and water vapor sorption that shine evidence on the lipophilicity and hydrophilicity of the NPs. These experiments showed that **Ph-PMO** is the most lipophilic structure, with a Henry constant towards cyclohexane four times higher than for silica, and twice as high as the other PMOs. Unsurprisingly, the hydrophilicity of silica is twice higher than for the other PMOs, which are however able to fully fill their pores with water at high relative pressure.

The chemistry of nanoPMOs is still in its infancy, owing to the potentially infinite variety of structures that may be obtained by varying the nature of the precursor and the synthetic conditions. By adequately designing the organic linker in the precursor, the interfacial properties may be finely tuned to enhance the encapsulation of drugs for nanomedicine, or the entrapment of molecules for water treatment.

References:

[1] N. Mizoshita, T. Tani, S. Inagaki, Syntheses{,} properties and applications of periodic mesoporous organosilicas prepared from bridged organosilane precursors, Chem. Soc. Rev. 40 (2011) 789–800. https://doi.org/10.1039/C0CS00010H.

[2] P. Van Der Voort, D. Esquivel, E. De Canck, F. Goethals, I. Van Driessche, F.J. Romero-Salguero, Periodic Mesoporous Organosilicas: from simple to complex bridges; a comprehensive overview of functions{,} morphologies and applications, Chem. Soc. Rev. 42 (2013) 3913–3955. https://doi.org/10.1039/C2CS35222B.

[3] A.M. Kaczmarek, P. Van Der Voort, Light-Emitting Lanthanide Periodic Mesoporous Organosilica (PMO) Hybrid Materials, Materials (Basel). 13 (2020). https://doi.org/10.3390/ma13030566.

[4] H. Li, D. Shen, H. Lu, F. Wu, X. Chen, R. Pleixats, J. Pan, The synthetic approaches, properties, classification and heavy metal adsorption applications of periodic mesoporous organosilicas, Sep. Purif. Technol. 277 (2021) 119453. https://doi.org/https://doi.org/10.1016/j.seppur.2021.119453.

[5] B. Karimi, N. Ganji, O. Pourshiani, W.R. Thiel, Periodic mesoporous organosilicas (PMOs): From synthesis strategies to applications, Prog. Mater. Sci. 125 (2022) 100896. https://doi.org/https://doi.org/10.1016/j.pmatsci.2021.100896.

[6] J.G. Croissant, X. Cattoën, M. Wong Chi Man, J.-O. Durand, N.M. Khashab, Syntheses and applications of periodic mesoporous organosilica nanoparticles, Nanoscale. 7 (2015) 20318–20334. https://doi.org/10.1039/c5nr05649g.

[7] B. Guan, Y. Cui, Z. Ren, Z. Qiao, L. Wang, Y. Liu, Q. Huo, Highly ordered periodic mesoporous organosilica nanoparticles with controllable pore structures, Nanoscale. 4 (2012) 6588–6596. https://doi.org/10.1039/C2NR31662E.

[8] S. Chinnathambi, F. Tamanoi, Recent Development to Explore the Use of Biodegradable Periodic Mesoporous Organosilica (BPMO) Nanomaterials for Cancer Therapy, Pharmaceutics. 12 (2020). https://doi.org/10.3390/pharmaceutics12090890.

[9] J.G. Croissant, Y. Fatieiev, K. Julfakyan, J. Lu, A.-H. Emwas, D.H. Anjum, H. Omar, F. Tamanoi, J.I. Zink, N.M. Khashab, Biodegradable Oxamide-Phenylene-Based Mesoporous Organosilica Nanoparticles with Unprecedented Drug Payloads for Delivery in Cells, Chem. – A Eur. J. 22 (2016) 14806–14811. https://doi.org/10.1002/chem.201601714.

[10] J. Croissant, X. Cattoën, M. Wong Chi Man, A. Gallud, L. Raehm, P. Trens, M. Maynadier, J.-

O. Durand, Biodegradable Ethylene-Bis (Propyl) Disulfide-Based Periodic Mesoporous Organosilica Nanorods and Nanospheres for Efficient In-Vitro Drug Delivery, Adv. Mater. 26 (2014) 6174–6180. https://doi.org/https://doi.org/10.1002/adma.201401931.

[11] C. Urata, H. Yamada, R. Wakabayashi, Y. Aoyama, S. Hirosawa, S. Arai, S. Takeoka, Y. Yamauchi, K. Kuroda, Aqueous Colloidal Mesoporous Nanoparticles with Ethenylene-Bridged Silsesquioxane Frameworks, J. Am. Chem. Soc. 133 (2011) 8102–8105. https://doi.org/10.1021/ja201779d.

[12] F. Tamanoi, S. Chinnathambi, M. Laird, A. Komatsu, A. Birault, T. Takata, T.L. Doan, N.X. Mai, A. Raitano, K. Morrison, M. Suzuki, K. Matsumoto, Construction of Boronophenylalanine-Loaded Biodegradable Periodic Mesoporous Organosilica Nanoparticles for BNCT Cancer Therapy, Int. J. Mol. Sci. 22 (2021). https://doi.org/10.3390/ijms22052251.

[13] N.X.D. Mai, Y.T. Dang, H.K.T. Ta, J.-S. Bae, S. Park, B.T. Phan, F. Tamanoi, T.L.H. Doan, Reducing particle size of biodegradable nanomaterial for efficient curcumin loading, J. Mater. Sci. 56 (2021) 3713–3722. https://doi.org/10.1007/s10853-020-05504-7.

[14] N.X.D. Mai, T.-H.T. Nguyen, D.H. Nguyen, L.H.T. Nguyen, H.T. Nguyen, T.B. Phan, F. Tamanoi, L.B. Vong, T.L.H. Doan, Engineering biodegradable periodic mesoporous functionalized-organosilica nanocarriers for efficient paclitaxel delivery, Colloids Surfaces A Physicochem. Eng. Asp. 656 (2023) 130405. https://doi.org/https://doi.org/10.1016/j.colsurfa.2022.130405.

[15] N. Pal, J.-H. Lee, E.-B. Cho, Recent Trends in Morphology-Controlled Synthesis and Application of Mesoporous Silica Nanoparticles, Nanomaterials. 10 (2020) 2122. https://doi.org/10.3390/nano10112122.

[16] M. Vafaeezadeh, W.R. Thiel, Periodic Mesoporous Organosilica Nanomaterials with Unconventional Structures and Properties, Chem. – A Eur. J. n/a (2023) e202204005. https://doi.org/https://doi.org/10.1002/chem.202204005.

[17] Y. Fatieiev, J.G. Croissant, K. Alamoudi, N.M. Khashab, Cellular Internalization and Biocompatibility of Periodic Mesoporous Organosilica Nanoparticles with Tunable Morphologies: From Nanospheres to Nanowires, Chempluschem. 82 (2017) 631–637. https://doi.org/10.1002/cplu.201600560.

[18] F. Chen, M. Ma, J. Wang, F. Wang, S.-X. Chern, E.R. Zhao, A. Jhunjhunwala, S. Darmadi, H. Chen, J. V Jokerst, Exosome-like silica nanoparticles: a novel ultrasound contrast agent for stem cell imaging, Nanoscale. 9 (2017) 402–411. https://doi.org/10.1039/C6NR08177K.

[19] S. Omar, R. Abu-Reziq, Highly Active Ruthenium Catalyst Supported on Magnetically Separable Mesoporous Organosilica Nanoparticles, Appl. Sci. 10 (2020). https://doi.org/10.3390/app10175769.

[20] M. Jahns, D.P. Warwas, M.R. Krey, K. Nolte, S. König, M. Fröba, P. Behrens, Nanoporous hybrid core–shell nanoparticles for sequential release, J. Mater. Chem. B. 8 (2020) 776–786. https://doi.org/10.1039/C9TB01846H.

[21] G. Tao, Z. Bai, Y. Chen, H. Yao, M. Wu, P. Huang, L. Yu, J. Zhang, C. Dai, L. Zhang, Generic synthesis and versatile applications of molecularly organic–inorganic hybrid mesoporous organosilica nanoparticles with asymmetric Janus topologies and structures, Nano Res. 10 (2017) 3790–3810. https://doi.org/10.1007/s12274-017-1592-5.

[22] S. Teng, Y. Han, Y. Hu, J. Li, M. Wang, Z. Guo, W. Yang, Swellable hollow periodic mesoporous organosilica capsules with ultrahigh loading capacity for hydrophobic drugs, J. Colloid Interface Sci. 630 (2023) 266–273. https://doi.org/https://doi.org/10.1016/j.jcis.2022.10.017.

[23] K. Zeng, L. Ma, W. Yang, S. Lei, M. Wang, Y. You, Y. Zhao, X. Ge, Biodegradable nano-

organosilica gene carrier for high-efficiency gene transfection, J. Mater. Chem. B. 8 (2020) 2483–2494. https://doi.org/10.1039/D0TB00108B.

[24] B. Marciniec, H. Maciejewski, J. Guliński, L. Rzejak, Metathesis of silicon containing olefins: II. Synthesis of 1,2-bis(silyl)ethenes by metathesis of vinylsilanes, J. Organomet. Chem. 362 (1989) 273–279. https://doi.org/https://doi.org/10.1016/0022-328X(89)87248-1.

[25] A. Birault, E. Molina, C. Carcel, J. Bartlett, N. Marcotte, G. Toquer, P. Lacroix-Desmazes, C. Gerardin, M. Wong Chi Man, Synthesis of lamellar mesostructured phenylene-bridged periodic mesoporous organosilicas (PMO) templated by polyion complex (PIC) micelles, J. Sol-Gel Sci. Technol. 89 (2019) 189–195. https://doi.org/10.1007/s10971-018-4667-1.

[26] R. Alvarado Meza, T. Santori, X. Cattoën, A kinetic approach to the mechanism of formation of mesoporous silica nanoparticles, J. Sol-Gel Sci. Technol. (2023). https://doi.org/10.1007/s10971-023-06130-w.

[27] F. Rouquerol, J. Rouquerol, K. Sing, CHAPTER 1 - Introduction, in: F. Rouquerol, J. Rouquerol, K.B.T.-A. by P. and P.S. Sing (Eds.), Academic Press, London, 1999: pp. 1–26. https://doi.org/https://doi.org/10.1016/B978-012598920-6/50002-6.

[28] V.H. Nguyen, A. Ibanez, M. Salaün, S. Kodjikian, P. Trens, X. Cattoën, Synthesis and properties of porous ester-silica nanoparticles, Microporous Mesoporous Mater. 317 (2021) 110991. https://doi.org/10.1016/j.micromeso.2021.110991.

[29] D. Aggad, C.M. Jimenez, S. Dib, J.G. Croissant, L. Lichon, D. Laurencin, S. Richeter, M. Maynadier, S.K. Alsaiari, M. Boufatit, L. Raehm, M. Garcia, N.M. Khashab, M. Gary-Bobo, J.-O. Durand, Gemcitabine Delivery and Photodynamic Therapy in Cancer Cells via Porphyrin-Ethylene-Based Periodic Mesoporous Organosilica Nanoparticles, ChemNanoMat. 4 (2018) 46–51. https://doi.org/https://doi.org/10.1002/cnma.201700264.

[30] M. Varache, I. Bezverkhyy, L. Saviot, F. Bouyer, F. Baras, F. Bouyer, Optimization of MCM-41 type silica nanoparticles for biological applications: Control of size and absence of aggregation and cell cytotoxicity, J. Non. Cryst. Solids. 408 (2015) 87–97. https://doi.org/https://doi.org/10.1016/j.jnoncrysol.2014.10.020.

[31] F. Catalano, P.P. Pompa, Design Rules for Mesoporous Silica toward the Nanosize: A Systematic Study, ACS Appl. Mater. Interfaces. 11 (2019) 47237–47246. https://doi.org/10.1021/acsami.9b16135.

[32] T. Ribeiro, A.S. Rodrigues, S. Calderon, A. Fidalgo, J.L.M. Gonçalves, V. André, M. Teresa Duarte, P.J. Ferreira, J.P.S. Farinha, C. Baleizão, Silica nanocarriers with user-defined precise diameters by controlled template self-assembly, J. Colloid Interface Sci. 561 (2020) 609–619. https://doi.org/https://doi.org/10.1016/j.jcis.2019.11.036.

[33] K. Bürglová, A. Noureddine, J. Hodačová, G. Toquer, X. Cattoën, M. Wong Chi Man, A General Method for Preparing Bridged Organosilanes with Pendant Functional Groups and Functional Mesoporous Organosilicas, Chem. Eur. J. 20 (2014) 10371–10382. https://doi.org/10.1002/chem.201403136.

[34] J. Lu, M. Liong, Z. Li, J.I. Zink, F. Tamanoi, Biocompatibility, Biodistribution, and Drug-Delivery Efficiency of Mesoporous Silica Nanoparticles for Cancer Therapy in Animals, Small. 6 (2010) 1794–1805. https://doi.org/https://doi.org/10.1002/smll.201000538.

[35] X. Liu, H. Wang, T. Li, H. Zheng, Y. Xu, J. Chen, J. Wang, Multipodal mesoporous silica hollow spheres: Branched hierarchical nanostructure by region-selective self-assembly, J. Colloid Interface Sci. 579 (2020) 21–27. https://doi.org/https://doi.org/10.1016/j.jcis.2020.06.063.

[36] J. Croissant, X. Cattoën, M. Wong Chi Man, P. Dieudonné, C. Charnay, L. Raehm, J.-O. Durand, One-Pot Construction of Multipodal Hybrid Periodic Mesoporous Organosilica Nanoparticles with Crystal-Like Architectures, Adv. Mater. 27 (2015) 145–149.

https://doi.org/10.1002/adma.201404226.

[37] J.G. Croissant, Y. Fatieiev, H. Omar, D.H. Anjum, A. Gurinov, J. Lu, F. Tamanoi, J.I. Zink, N.M. Khashab, Periodic Mesoporous Organosilica Nanoparticles with Controlled Morphologies and High Drug/Dye Loadings for Multicargo Delivery in Cancer Cells, Chem. – A Eur. J. 22 (2016) 9607–9615. https://doi.org/10.1002/chem.201600587.

[38] S. Inagaki, S. Guan, T. Ohsuna, O. Terasaki, An ordered mesoporous organosilica hybrid material with a crystal-like wall structure, Nature. 416 (2002) 304–307. https://doi.org/10.1038/416304a.

[39] F.D. Osterholtz, E.R. Pohl, Kinetics of the hydrolysis and condensation of organofunctional alkoxysilanes: a review, J. Adhes. Sci. Technol. 6 (1992) 127–149. https://doi.org/10.1163/156856192X00106.

[40] A.P. Bento, F.M. Bickelhaupt, Nucleophilic Substitution at Silicon (SN2@Si) via a Central Reaction Barrier, J. Org. Chem. 72 (2007) 2201–2207. https://doi.org/10.1021/jo070076e.

[41] I. Langmuir, The adsorption of gases on plane surfaces of glass, mica and platinum, J. Am. Chem. Soc. 40 (1918) 1361–1403. https://doi.org/10.1021/ja02242a004.

[42] S. Nethaji, A. Sivasamy, A.B. Mandal, Adsorption isotherms, kinetics and mechanism for the adsorption of cationic and anionic dyes onto carbonaceous particles prepared from Juglans regia shell biomass, Int. J. Environ. Sci. Technol. 10 (2013) 231–242. https://doi.org/10.1007/s13762-012-0112-0.

[43] H.. Freundlich, Concerning Adsorption in Solutions., Zeitschrift Fur Phys. Chemie-Stochiometrie Und Verwandtschaftslehre. 57 (1906) 385–470.

[44] Qurrat-ul-Ain, J. Khatoon, M.R. Shah, M.I. Malik, I.A.T. Khan, S. Khurshid, R. Naz, Convenient pH-responsive removal of Acid Black 1 by green l-histidine/iron oxide magnetic nanoadsorbent from water: performance and mechanistic studies, RSC Adv. 9 (2019) 2978–2996. https://doi.org/10.1039/C8RA09279F.

[45] H. Han, W. Wei, Z. Jiang, J. Lu, J. Zhu, J. Xie, Removal of cationic dyes from aqueous solution by adsorption onto hydrophobic/hydrophilic silica aerogel, Colloids Surfaces A Physicochem. Eng. Asp. 509 (2016) 539–549. https://doi.org/https://doi.org/10.1016/j.colsurfa.2016.09.056.

[46] A. Noureddine, P. Trens, G. Toquer, X. Cattoën, M. Wong Chi Man, Tailoring the Hydrophilic/Lipophilic Balance of Clickable Mesoporous Organosilicas by the Copper-Catalyzed Azide--Alkyne Cycloaddition Click-Functionalization, Langmuir. 30 (2014) 12297–12305. https://doi.org/10.1021/la503151w.

[47] K. Morishige, Y. Nakamura, Nature of Adsorption and Desorption Branches in Cylindrical Pores, Langmuir. 20 (2004) 4503–4506. https://doi.org/10.1021/la030414g.

[48] P. Trens, N. Tanchoux, P.-M. Papineschi, D. Maldonado, F. di Renzo, F. Fajula, Confinements effects in MCM-41-type materials: Comparison of the energetics of n-hexane and 1-hexene adsorption, Microporous Mesoporous Mater. 86 (2005) 354–363. https://doi.org/https://doi.org/10.1016/j.micromeso.2005.07.039.

[49] P. Trens, N. Tanchoux, A. Galarneau, D. Brunel, B. Fubini, E. Garrone, F. Fajula, F. Di Renzo, A Macrothermodynamic Approach to the Limit of Reversible Capillary Condensation, Langmuir. 21 (2005) 8560–8564. https://doi.org/10.1021/la0507838.

[50] K. Morishige, Adsorption hysteresis in ordered mesoporous silicas, Adsorption. 14 (2008) 157–163. https://doi.org/10.1007/s10450-007-9086-5.

[51] P. Trens, N. Tanchoux, D. Maldonado, A. Galarneau, F. Di Renzo, F. Fajula, Study of n-hexane adsorption in MCM-41 mesoporous materials: a scaling effect approach of capillary

condensation processes, New J. Chem. 28 (2004) 874–879. https://doi.org/10.1039/B401094A.

[52] V.T. Lam, G.C. Benson, Surface tensions of binary liquid systems. I. Mixtures of nonelectrolytes, Can. J. Chem. 48 (1970) 3773–3781. https://doi.org/10.1139/v70-637.

[53] C. Picard, V. Gérard, L. Michel, X. Cattoën, E. Charlaix, Dynamics of heterogeneous wetting in periodic hybrid nanopores, J. Chem. Phys. 154 (2021) 164710. https://doi.org/10.1063/5.0044391.

[54] F. Lin, X. Meng, K. Tang, L. Wu, R. Yuan, L. Liao, Structure modulation of periodic mesoporous organosilicas with organic salts, J. Mater. Sci. 56 (2021) 13590–13603. https://doi.org/10.1007/s10853-021-06191-8.

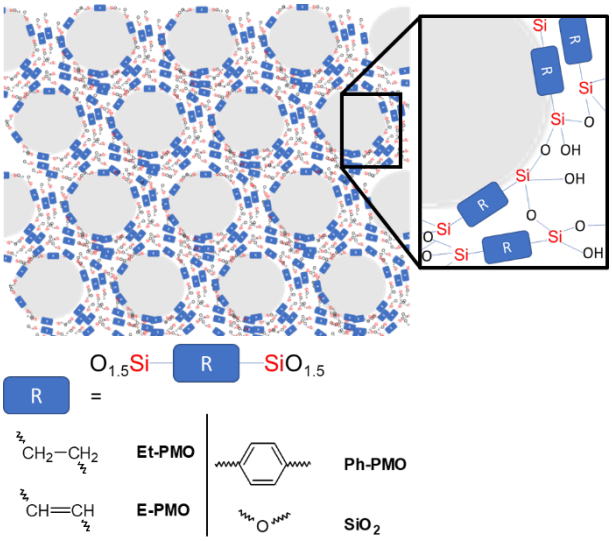

Figure 1: Schematic representation of the structure or PMOs, depicting the three organic linkers R studied in this report. The grey holes represent the pores of the structure.

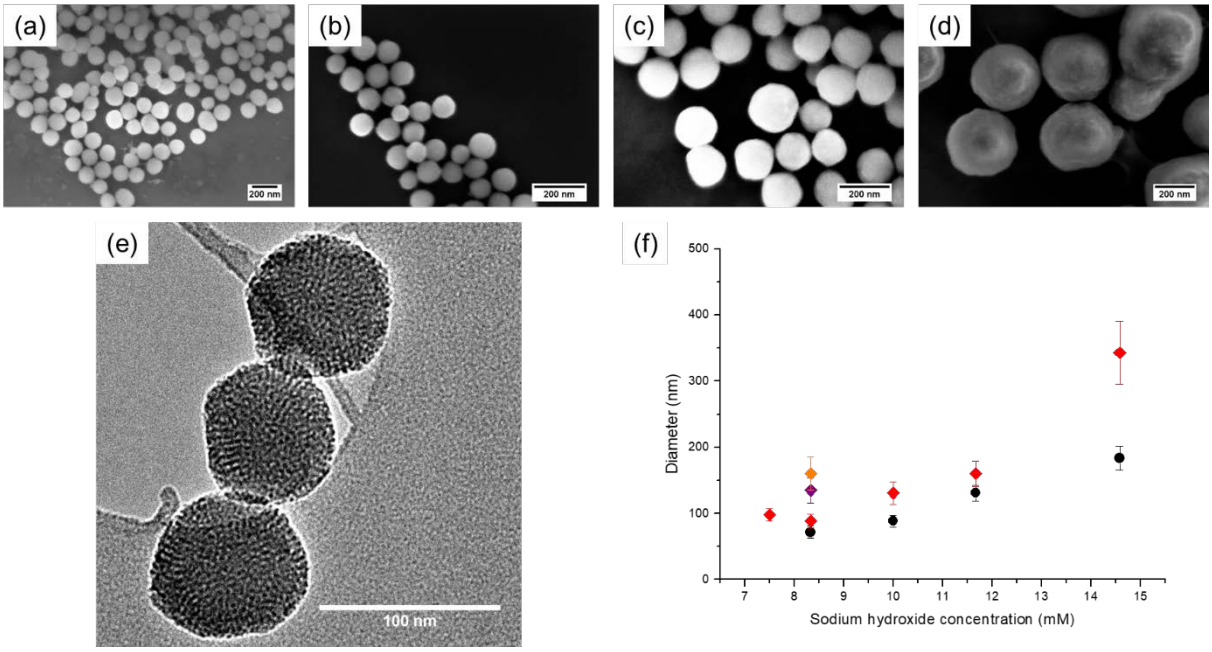

Figure 2: SEM micrographs of **Et-PMO** NPs obtained upon increasing sodium hydroxide concentration. (a): 8.3 mM; (b): 10 mM; (c): 11.7 mM; (d): 14.6 mM. with [**Et**] = 18 mM. Scale bars 200 nm. (e) TEM micrograph of **Et-PMO** obtained with [NaOH] = 8.3 mM and [**Et**] = 18 mM, Scale bar 100 nm; (f) Evolution of the mean diameter depending on the NaOH concentration: for [**Et**] = (black) 6.8 and (red) 18 mM and with [**Et**] = 18 mM, and [NaCl] = (purple) 4.2; (orange) 8.3 mM.

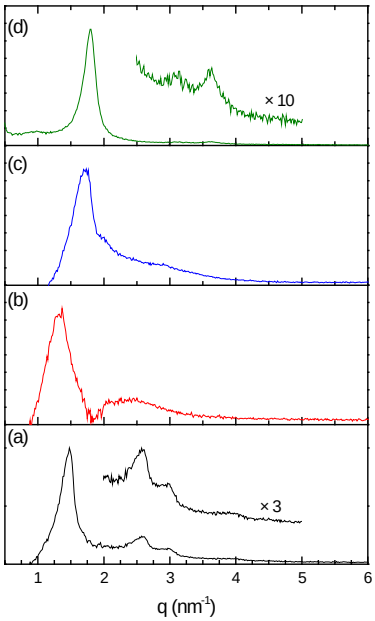

Figure 3: X-ray diffractograms of **PMO** and SiO_2 NPs with size of 90 nm for (a) **E-PMO** (flakes obtained with [NaOH] = 6.7 mM); (b) **Et-PMO**; (c) **Ph-PMO**; (d) SiO_2.

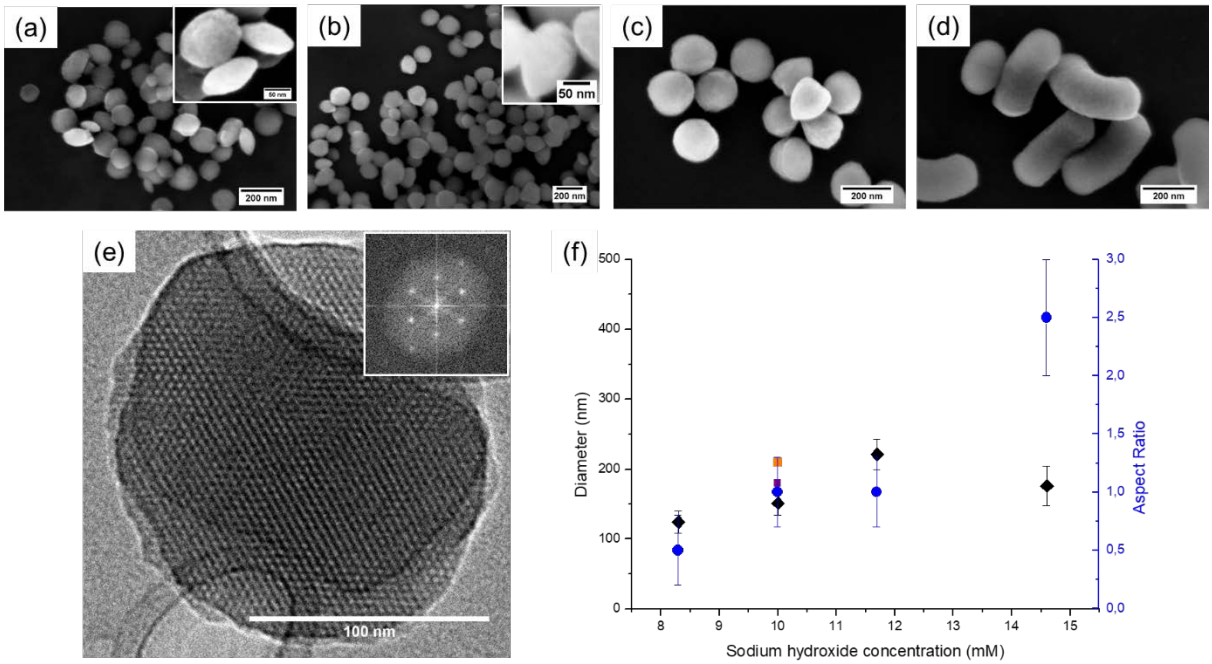

Figure 4: SEM micrographs of **E-PMO** NPs upon increasing sodium hydroxide concentration for [**E**] = 18 mM. (a): 8.3 mM; (b): 10 mM; (c): 11.7 mM; (d): 14.6 mM. (e) TEM micrograph of **E-PMO** synthesized with [**E**] = 18 mM and [NaOH] = 10 mM. Inset: FFT of the image, evidencing the hexagonal arrangement of the pores; (f) Evolution of (black) the mean diameter and (blue) the aspect ratio depending on the NaOH concentration for [**E**] = 18 mM. Diameter of the **E-PMO** NPs with [NaCl] = (purple) 5; (orange) 10 mM.

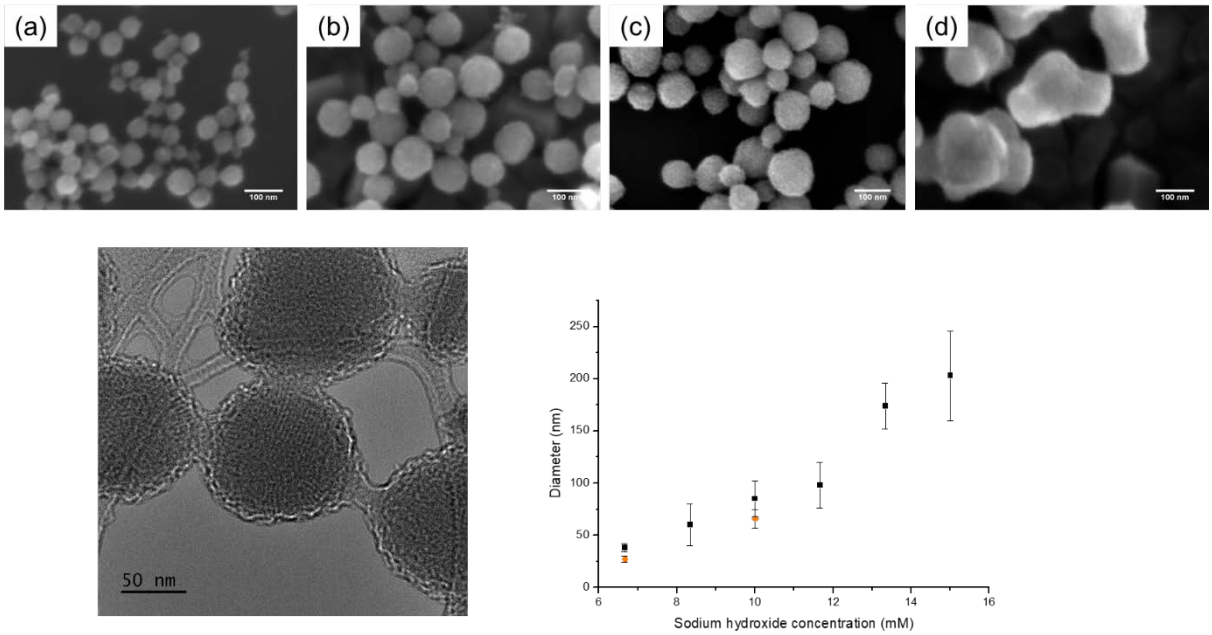

Figure 5: SEM micrographs of **Ph-PMO** NPs upon increasing sodium hydroxide concentration for [**Ph**] = 18 mM. (a): 8.3 mM; (b): 10 mM; (c): 11.7 mM; (d): 15.0 mM. (e) TEM micrographs of Ph-PMO NPs obtained with [**Ph**] = 18 mM and [NaOH] = 11.7 mM. (f) Evolution of the mean diameter depending on the NaOH concentration. Diameter of the **Ph-PMO** NPs with addition of salt [NaCl] = (orange) 10 mM.

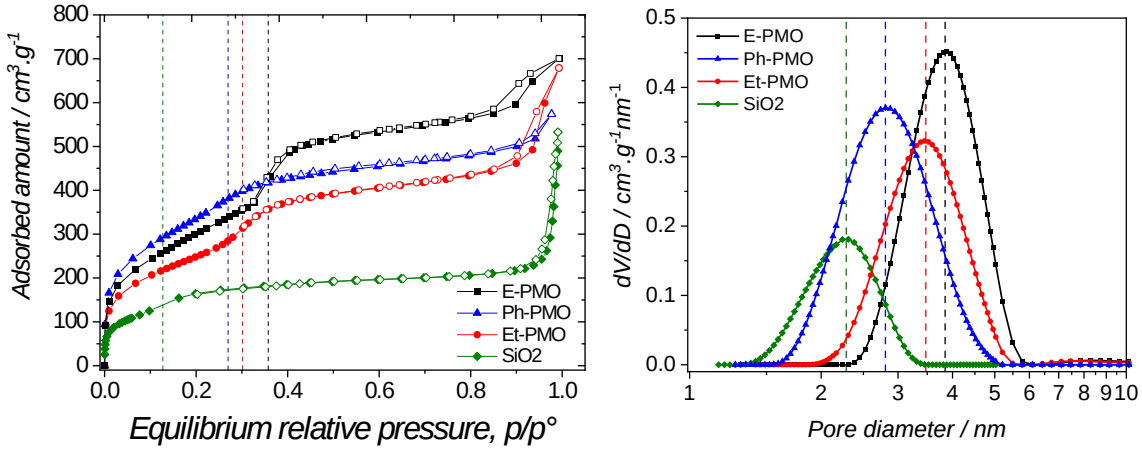

Figure 6: (left) N_2-sorption isotherms and (right) DFT pore size distributions of (black) **E-PMO**; (red) **Et-PMO**; (blue) **Ph-PMO**; (green) **SiO_2** NPs. The pore size distributions plots have been derived using the adsorption branches of the sorption isotherms.

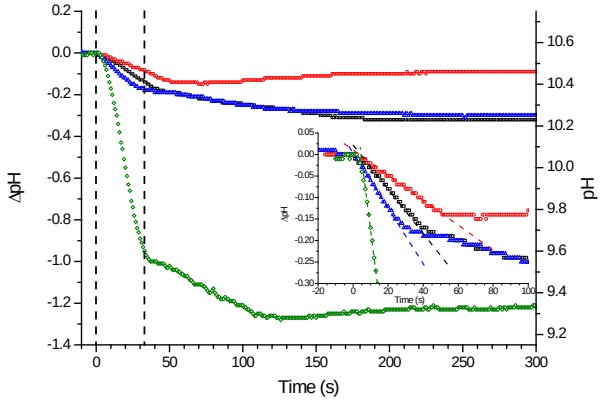

Figure 7: Evolution of the pH during the early stages of **PMO** formation, with $[\mathbf{Si}]_0$ = 36 mM and $[NaOH]_0$ = 10 mM, [CTAB] = 5.7 mM, for (black) **E**, (red) **Et**, (blue) **Ph**, (green) TEOS.

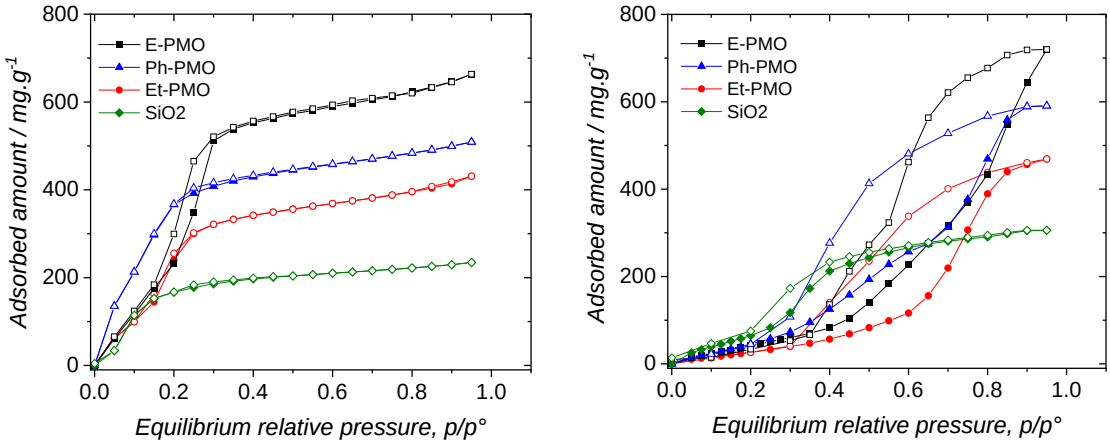

Figure 8: (left) cyclohexane and (right) water adsorption isotherms at 298 K for (black) **E-PMO** (red) **Et-PMO**, (blue) **Ph-PMO** and (green) **SiO_2**. The inset for water adsorption is a magnification of the low-pressure part of the isotherm.

Sample	S_{BET} / m^2 g^{-1}	V_p / $cm^3.g^{-1}$	D_p / nm	$K_{H\ C6H12}$ / $cm^3.g^{-1}$	$K_{H\ H2O}$ / $cm^3.g^{-1}$
E	1127	0.823	3.8	1240	288
Et	916	0.626	3.4	1237	214
Ph	1144	0.702	2.9	2710	321
SiO_2	519	0.304	2.3	680	510

Table 1. Textural properties by N_2-sorption isotherms at 77 K, and Henry constants for water and cyclohexane at 298 K.

Precursor	k_{app} (s^{-1})	ΔpH[a]	conversion (%)[b]
E	$1.1\ 10^{-2}$	-0.19	9.8
Et	$6.5\ 10^{-3}$	-0.14	8.0
Ph	$1.5\ 10^{-2}$	-0.19	9.8
TEOS	$8.2\ 10^{-2}$	-1.0	25

Table 2: Apparent first order kinetic constants calculated in the first linear regime for the hydrolysis of **E**, **Et, Ph** and TEOS with [Si] = 36 mM, [NaOH] = 10 mM, [CTAB] = 5.7 mM at 80 °C. [a] pH difference between the start and the cloud point. [b] Amount of silicon atom featuring a silanolate group at the cloud point, determined from the pH difference.

Sample	Langmuir model				Freundlich model		
	q_{max} / mg g^{-1}	K_L / L g^{-1}	R_L	R^2	K_F / $mg^{1-1/n}.L^{1/n}.g^{-1}$	n	R^2
E	361	5.95	$0.08 < R_L < 0.89$	0.9875	306	2.00	0.9753
Et	251	4.34	$0.10 < R_L < 0.92$	0.9311	169	2.52	0.9834
Ph	548	30.6	$0.02 < R_L < 0.62$	0.9958	611	2.65	0.9164
SiO_2	282	3.61	$0.12 < R_L < 0.93$	0.9883	234	1.65	0.9074

Table 3. Langmuir and Freundlich parameters obtained after RB adsorption on the different materials.

Periodic mesoporous organosilica nanoparticles: morphology control and sorption properties

Xavier Cattoën,[a,*] Stéphanie Kodjikian,[a] and Philippe Trens[b]

[a] Univ. Grenoble Alpes, CNRS, Grenoble INP, Institut Néel, 38000 Grenoble, France.
[b] ICGM University of Montpellier, CNRS, ENSCM, Montpellier, France
xavier.cattoen@neel.cnrs.fr

stephanie.kodjikian@neel.cnrs.fr

Philippe.Trens@enscm.fr

ELECTRONIC SUPPLEMENTARY INFORMATION

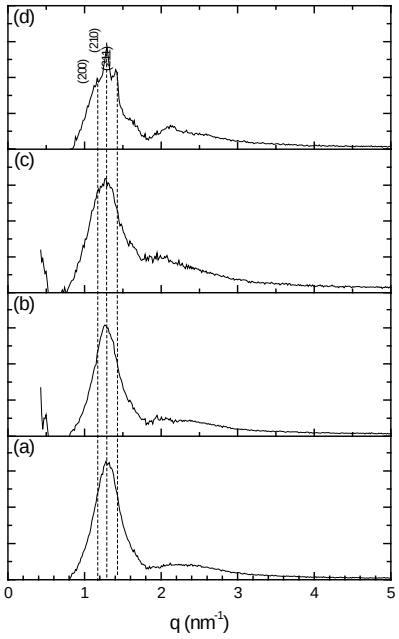

Figure S1: X-ray diffractograms of **Et-PMO** NPs obtained for [**Et**] = 18 mM with varying NaOH concentrations (a): 8.3 mM; (b): 10 mM; (c): 11.7 mM; (d): 14.6 mM.

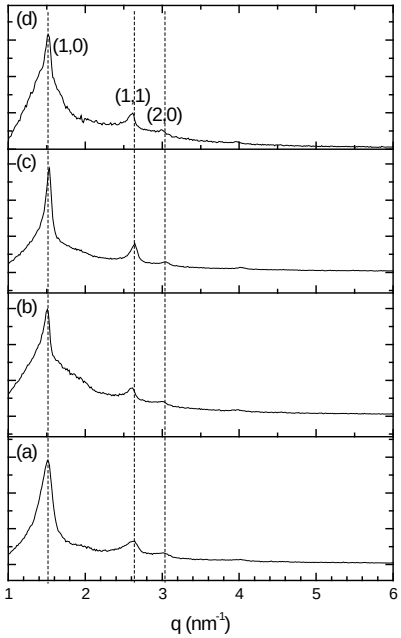

Figure S2: X-ray diffractograms of **E-PMO** NPs obtained for [**E**] = 18 mM with varying NaOH concentrations (a): 8.3 mM; (b): 10 mM; (c): 11.7 mM; (d): 14.6 mM.

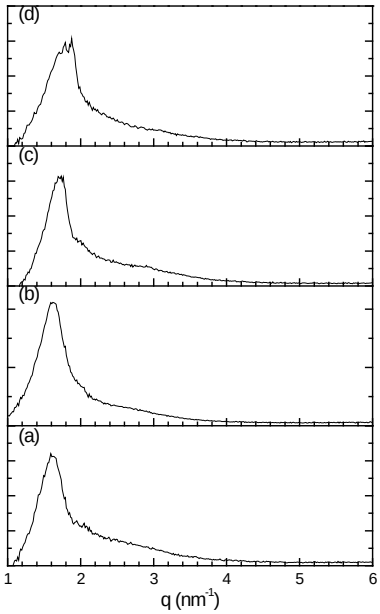

Figure S3: X-ray diffractograms of **Ph-PMO** NPs obtained for [**Ph**] = 18 mM with varying NaOH concentrations (a): 8.3 mM; (b): 10 mM; (c): 11.7 mM; (d): 15 mM.

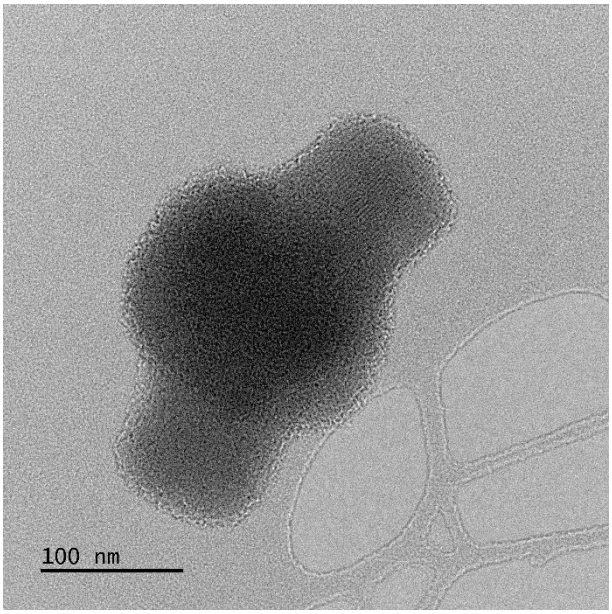

Figure S4: TEM micrographs of a **Ph-PMO** NP obtained with [NaOH] = 15 mM.

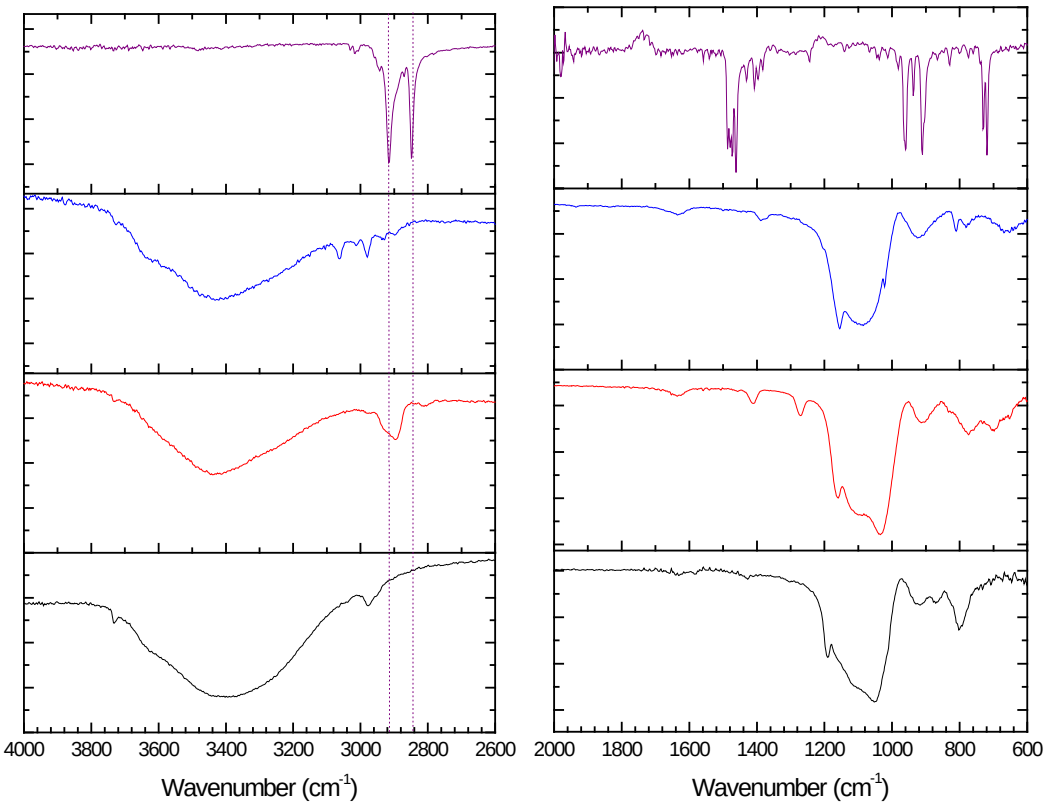

Figure S5: Compared FTIR spectra of (black) **E-PMO**; (red) **Et-PMO** and (blue) **Ph-PMO** compared to (purple) CTAB. The dotted lines highlight the position of the CH_2 stretching bands of CTAB, evidencing the complete removal of the surfactant in all cases.

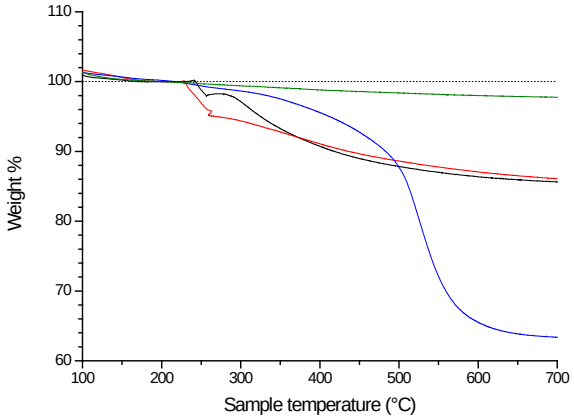

Figure S6: Thermogravimetric analysis of nanoPMOs: (black) **E-PMO**, (red) **Et-PMO**, (blue) **Ph-PMO**, (green) SiO_2. The corresponding weight losses at 700 °C are: for **E-PMO**: 14.4% (15.0%); **Et-PMO**: 13.9% (13.3%); **Ph-PMO**: 31.3% (33.3%); SiO_2: 2.3% (0.0%). The values between brackets represent the theoretical values for the formulae $O_{1.5}SiRSiO_{1.5}$, with R = CH=CH, CH_2-CH_2, C_6H_4 and O, respectively.

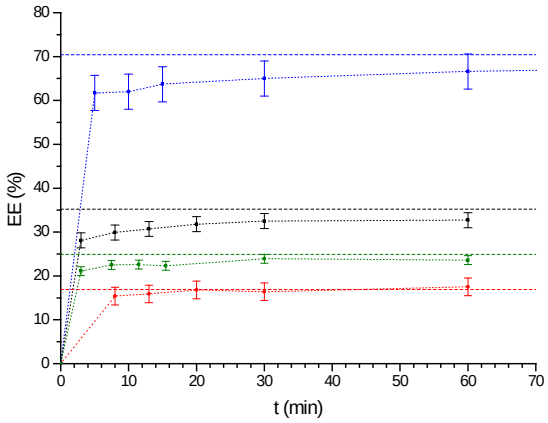

Figure S7: Adsorption kinetics of RB in (black) **E-PMO**, (red) **Et-PMO**; (blue) **Ph-PMO** and (green) **SiO_2**. [NP] = 1.0 mg/mL; [RhB] = 0.5 mg/mL, EE = encapsulation efficiency.

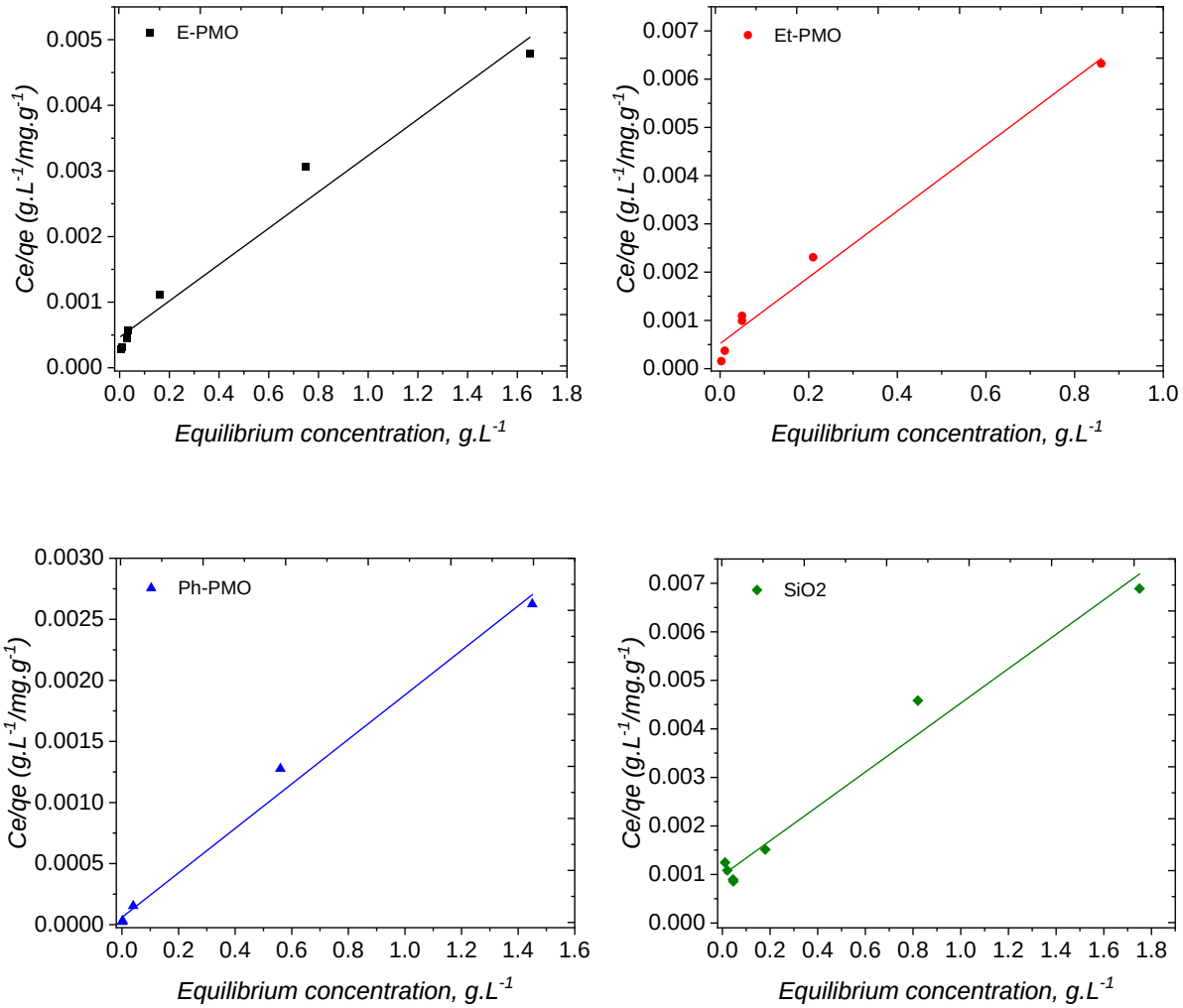

Figure S8. Linear Langmuir plots obtained from RB adsorption on the different materials.

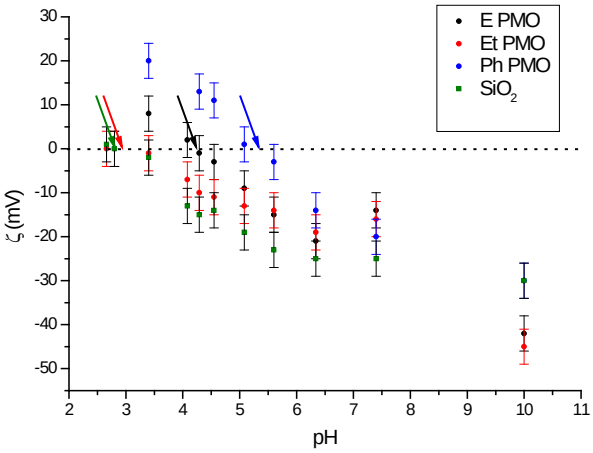

Figure S9: Representative evolution of the Zêta potential with pH for (black) **E-PMO**, (red) **Et-PMO**, (blue) **Ph-PMO** and (green) silica. The representative point of zero charge (arrows) are *ca* 4.0, 3.0, 5.5 and 3.0, respectively.

Sample	A_T	B_T	R^2
E-PMO	398	445.7	0.9687
Et-PMO	9	77.0	0.8859
Ph-PMO	537461	37.5	0.9942
SiO_2	52	52.1	0.9879

Table S1. Temkin parameters obtained after rhodamine sorption on the different materials.

The Temkin isotherm model assumes that there is a linear decrease in the heat of adsorption of molecules in a layer as a function of temperature, and that there is a uniform distribution of binding energies.[45,46] This model investigates both the heat of adsorption and binding interactions.

$$q_e = \left[\frac{R_T}{B_T}\right] \ln A_T + \left[\frac{R_T}{B_T}\right] \ln[C_e] \quad (3)$$

The heat of adsorption is related to the Temkin constant B_T (J/mol), which is calculated from the slope of the linear plot of q_e versus lnC_e. The intercept of this Temkin isotherm plot gives the equilibrium binding constant (A_T, L/g), which is related to the maximum binding energy. Despite the rather high correlation coefficients obtained, the data could not be properly fitted by the Temkin model. The range of A_T and B_T values are unreasonably large for the results to be consistent.

Langmuir parameters	q_{max} / mg.g^{-1}	K_L / L mg^{-1}
Ph-PMO (this work)	548	0.03
MSA, Ref [45]	185	0.02

Table S2. Comparison of the Langmuir parameters obtained in our study and in ref [45].